THE JOURNAL OF PHYSICAL CHEMISTRY C

Article

pubs.acs.org/JPCC

Excess Sorption of Supercritical CO_2 within Cylindrical Silica Nanopores

M. Dolores Elola*,† and Javier Rodriguez†

†Departamento de Física, Comisión Nacional de Energía Atómica, Avenida Libertador 8250, 1429 Buenos Aires, Argentina

‡ECyT, UNSAM, Martín de Irigoyen 3100. 1650 San Martín Provincia de Buenos Aires Argentina

ABSTRACT: Using Molecular Dynamics simulations, we examine structural and dynamical properties of supercritical CO_2 confined within cylindrical hydrophobic nanopores of diameters 38 and 10 Å. Computer simulations were performed along the isotherm T = 315 K, spanning CO_2 densities from ρ/ρ_c = 2.22 down to ρ/ρ_c = 0.22. Radial and orientational distribution functions, analysis of interfacial dynamic properties, and estimatons for local diffusion and orientational relaxation times are presented. In agreement with previous experimental data, our simulation results reveal the presence of a dense phase adsorbed within the pores. The combination of low CO_2 bulk densities and narrow pores leads to $\rho_{int}/\rho_{blk} \approx$ 5-fold enhancement of the global density of the confined fluid. These density increments gradually become much less marked as the external phase becomes denser. Contrasting, in that latter limit, we found that the trapped fluid may become less dense than the bulk phase. Adsorption behavior of CO_2 onto hydrophilic-like and rugged pore surfaces were also exmined. In these cases, we observed a global slowdown in both translational and rotational motions for the trapped CO_2, the largest retardations being those associated with spatial domains of the fluid located near the silica interface.

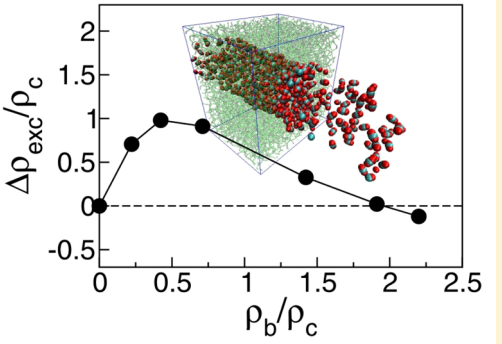

I. INTRODUCTION

Fluids under nanometric confinement may exhibit distinctive characteristics that contrast with those observed in bulk phases. A physical interpretation of these modifications is essential to understand how finite size effects affect the behavior of confined fluids.

Specifically, the study of the properties of supercritical CO_2 ($scCO_2$) within pores of nanometric dimensions has been the focus of several investigations in recent years.[1−7] The analysis of this particular system is relevant for fluid chromatography and subsurface carbon storage technologies, among other important applications. The current high levels of CO_2 found in the atmosphere, along with the dramatic increments of carbon dioxide that are expected to be discharged in coming decades, motivate the efforts to mitigate global climate changes through carbon capture and sequestration.[8,9] A knowledge of the molecular details of CO_2-pore interactions is then critical for the design of improved carbon-capture systems.

Experimental techniques such as small-angle neutron scattering (SANS),[10,11] gravimetry,[3,12] and volumetric sorption[13,14] are usually employed to measure the properties of confined fluid phases. These experiments provide evidence that, at low fluid pressures and within narrow pores, the adsorbed phase is in a densified state; indicating that carbon storage is enhanced by sorption effects. On the other hand, the existence of a confined phase that is less dense than the corresponding external fluid was found at high bulk densities. Moreover, it has been reported that the maximum of the CO_2 adsorption occurs for smaller bulk densities when the pores become narrower.

In recent years, structural and dynamical behavior of simple fluids, such as argon, carbon dioxide, and H_2 next to silica surfaces have been investigated by computer simulations.[15−19] Specifically, $scCO_2$ has been examined at the vicinity of modified silica surfaces in slit-like geometries.[15] Simulation results indicate a CO_2 density enhancement near the hydroxylated silica surface sites, revealing a stronger adsorption affinity for these derivatized surfaces. Still, and to the best of our knowledge, a microscopic analysis of $scCO_2$ confined within cylindrical silica nanopores of different sizes has not been yet analyzed by computer simulations.

Melnichenko et al.[4] and Rother et al.,[5] have investigated the excess sorption isotherms of $scCO_2$ in mesoporous silica glasses with nominal pore sizes varying from 1.6 to 35 nm by gravimetry and SANS techniques over a wide range of densities (pressures) and temperatures. These experimental techniques provide valuable and accurate information about the sorption phase and the average fluid density inside the cavity, since they are model-independent. Although these results are obtained with a small degree of uncertainty, it is not possible to extract from them information about the local density fluctuations close to the pore walls, at a molecular microscopic level. A

Received: September 15, 2015
Revised: December 18, 2015

ACS Publications © XXXX American Chemical Society

DOI: 10.1021/acs.jpcc.5b09000
J. Phys. Chem. C XXXX, XXX, XXX−XXX

recent paper of Rother et al.,[6] presents experimental and simulation results that particularly focus on the characteristics of the $scCO_2$ sorption layer pinned to the pore walls in silica aerogel. Results show a similar behavior for these adsorbed layers than those previously described for the trapped CO_2, nevertheless, the $scCO_2$ sorption layer may be up to 3 times denser than the CO_2 bulk phase. Largely motivated by these previous interesting studies, in this work we will present results from Molecular Dynamics (MD) simulations that shed light on the behavior of $scCO_2$ confined within cylindrical silica nanopores of diameter sizes ranging between 1 and 4 nm.

The paper is organized as follows: in section II we describe the systems studied and the potential models, along with simulation details. In section III we present and discuss the results obtained for the structural and dynamical properties. We conclude in section IV with a summary of our main findings.

II. MODEL AND SIMULATION DETAILS

We carried out molecular dynamics simulations of systems composed of cylindrical pores with diameters D_p = 1 and 3.8 nm, filled with CO_2 at supercritical temperatures. All components of the simulated systems were modeled as a collection of interacting sites. The overall potential energy was considered as a sum of site−site, pairwise interactions combining dispersion (Lennard-Jones) and Coulomb contributions. To model inter and intramolecular interactions in CO_2 we adopted the two-site, EPM2 potential.[20] This force field was adjusted so as to accurately reproduce critical constants, namely ρ_c^{EPM2} = 0.45 g cm^{-3} and T_c^{EPM2} = 313 K. These numbers should be compared to the experimental values: ρ_c = 0.47 g cm^{-3} and T_c = 304 K. All simulated thermodynamic states were chosen along the T = 315 K isotherm, covering a range of CO_2 densities spanning between ρ/ρ_c = 0.22 (ρ = 0.1 g cm^{-3}) and ρ/ρ_c = 2.22 (ρ = 1.0 g cm^{-3}). Force field parameters for silica were taken from ref 21 and cross interactions between the pore and the supercritical phase were computed assuming the usual arithmetic and geometric means for length and energy parameters, respectively.

The preparation of the systems involved a sequential procedure which is described in detail in refs 22 and 23. Briefly, the cylindrical silica pore of D_p = 38 Å was built up from an amorphous silica rectangular block of linear dimensions L_x = L_y = 70 Å, L_{zp} = 50 Å. After proper equilibration at temperatures close to $T \approx$ 8000 K, the block was cooled down to ambient conditions, and molecules lying in the central cylindrical of diameter D_p were removed. Pores with diameters of 10 Å were also generated from similar blocks of linear dimensions L_x = L_y = 70 Å, L_{zp} = 50 Å. Finally, in order to mimick a hydrophobic environment, we simply turned off all partial charges in the original silica and oxygen sites so that only Lennard-Jones dispersive forces remained. No efforts were invested in reproducing experimental protocols to control the degree of hydrophobicity within the pores.

The final stage of sample preparation involved the incorporation of the supercritical carbon dioxide phase within the different pores. To do so, the latteral faces of the holed blocks were brought in contact with two adjacent, lateral, bulk-like CO_2 reservoirs that led to a periodically replicated, simulation box of linear dimensions L_x = L_y = 70 Å and L_z = 270 Å. From then on, the CO_2 supercritical phase was allowed to penetrate into the pores and re-equilibrate at T = 315 K for about 4 ns. During this period, the length of the simulation box along the z-axis was adjusted to set the pressure and local density away from the pore lateral faces to the CO_2 corresponding bulk values. Figure 1 shows snapshots of typical configurations captured during the MD simulations.

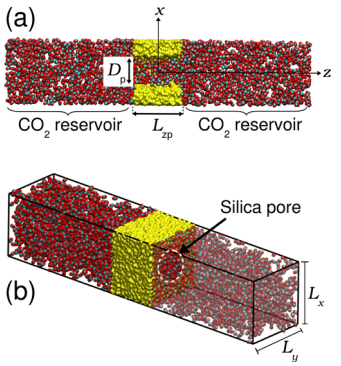

Figure 1. (a) Typical snapshot of the configuration of the system for D_p = 38 Å, showing the axes and the CO_2 reservoirs in contact with the silica pore. In panel b, a perspective view of the same system is shown.

All molecular dynamics (MD) trajectories were generated using the NAMD package[24] and corresponded to *NVT*, canonical runs. Short-ranged intermolecular forces were cut off at 13 Å, while the particle mesh Ewald (PME) method was implemented to handle long-range Coulomb forces. The equations of motion were integrated using a multiple time step integration scheme, with a time step of 1 fs for intramolecular modes and nonbonded short-ranged forces, and 2 fs for the rest of the Coulomb forces.

III. RESULTS

Structural Properties. *Spatial Correlations.* We will start our analysis by investigating the structural features of $scCO_2$ within the pores. In Figure 2, we present results for density profiles of CO_2 along the axial direction, namely:

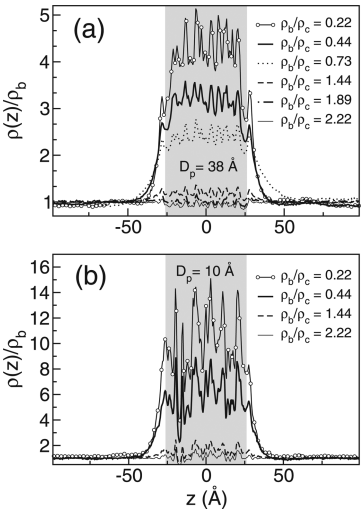

Figure 2. Local (normalized to ρ_b) densities of $scCO_2$ along the axial z axis, for the hydrophobic simulated pores at T = 315 K: (a) pore of diameter D_p = 38 Å; (b) small pore of D_p = 10 Å. Densities have been computed within an axial cylinder of diameter D_p and 200 Å length. The shaded region indicates the location of the silica pore.

DOI: 10.1021/acs.jpcc.5b09000
J. Phys. Chem. C XXXX, XXX, XXX−XXX

$$\rho(z) = \frac{1}{\pi R^2} \sum_i \langle \delta(z_i - z) \rangle_R \quad (1)$$

where z_i corresponds to the z-coordinate of the center of mass of the ith molecule and $\langle \cdots \rangle_R$ denotes an average restricted to those molecules with distances to the z-axis less than $R = D_p/2$.

As expected, at sufficiently long distances away from the pore rims—say $|z| \approx 30$ Å—all density profiles reach their corresponding bulk values (ρ_b). In contrast, within the interior of the pore, a density enhancement is clearly perceptible. Moreover, this increment looks much more pronounced, the lower the bulk density considered, attaining $\rho(z = 0)/\rho_b \approx 5$, for $\rho_b/\rho_c \approx 0.2$. The direct comparison between the results from panels (a) and (b) reveals the magnitude of pore size effects on the latter enhancements. Note that in passing from $D_p = 38$ Å down to $D_p = 10$ Å, the density inside the pore suffers an additional, 3-fold increment at low ρ_b. The plots shown in Figure 2 also reveal important fluctuations of the local densities along the z-axis, which are markedly larger, the smaller diameter of the pore. This feature is a natural consequence of the local rugosity of the pore walls, whose characteristic length scale remains comparable to the pore diameters. To assess how these surface effects extend within the interior of the pore, we examined local density fluctuations along radial directions, namely:

$$\rho(r) = \frac{1}{2\pi r L_{zp}} \sum_i \langle \delta(r_i - r) \rangle_R \quad (2)$$

where r_i corresponds to the distance of the ith site and the pore axis.

In Figure 3 panels a and b we present results for radial densities within pores of different diameters. In both cases, the profiles reveal a strongly adsorbed interfacial layer, located at approximately 4 Å inward from the pore wall. Interestingly, in the wider pore, the magnitudes of the corresponding peaks present only a modest 15% increment, as the bulk density changes in practically 1 order of magnitude; moreover, in the narrower pores, these increments are practically missing. Also note that the local densities of the adsorbed phases are comparable—or even surpass—typical values of CO_2 liquid phases in the vicinity of the triple point, that is, $\rho_{tp}/\rho_c \approx 2.5$. These values would suggest a surface-induced condensation phenomenon, characterized by a highly ordered, adsorbed layer. In addition to this dense adsorbed phase, all profiles in panel a show adjacent layers located ~6 Å inward from the pore wall, followed by smooth decays toward the centers of the pore. For $\rho_b \leq 1.5\ \rho_c$, the curves exhibit exponential-like decays as one moves toward the pore center with correlation length ξ. The length scale gauges the extent by which the coupling with the pore wall modifies the local density of CO_2. In Figure 4 we present results for ξ obtained from best fits the decays, for pores with $D_p = 38$ Å. Clearly, a maximum value $\xi \approx 16$ Å is reached for $\rho_b/\rho_c = 0.6$; interestingly, this density coincides with the one in which maximum augmentations in the local density around attractive solutes have been previously reported.[25−27]

The layered structures of CO_2 in narrower pores shown in Figure 3b differ from the previous description at a qualitative level. All plots look practically identical and are characterized by an adsorbed layer twice as dense as the ones found in wider pores. Moreover, the width of the pore is comparable to the molecular size, so the center of the pores looks practically devoid of CO_2. The latter results would underline the

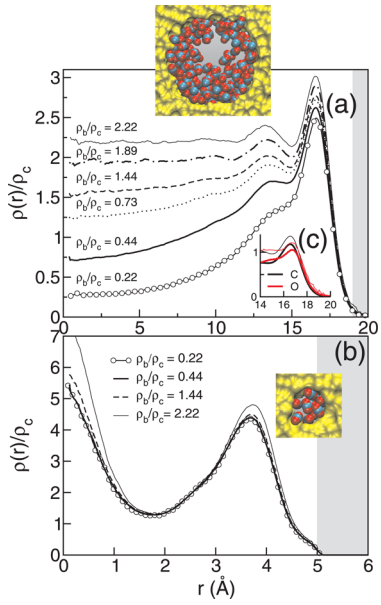

Figure 3. Local (normalized to ρ_c) density of CO_2 within hydrophobic pores, along the cylindrical radial direction. Densities on panels a and b correspond to the pores of diameter 38 and 10 Å, respectively. The inset (c) shows a detail of the local densities associated with C (black) and O sites (red) of CO_2, within the largest pore, for $\rho_b/\rho_c = 0.44$ (thick lines) and 2.22 (thin lines). The shaded region represents the location of the silica wall; the snapshots depict a cut of the corresponding systems over the central pore region of width $\Delta z = 8$ Å, for $\rho_b/\rho_c = 0.44$.

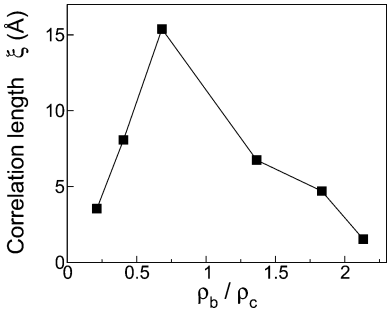

Figure 4. Correlation length, ξ, obtained from fits of the decay of $\rho(r)$ to an exponential function of the form: $\rho(r) \approx \rho_b + \delta\rho \exp(-r/\xi)$, as a function of the reduced bulk density, ρ_b/ρ_c, for confined $scCO_2$ within the pore of size $D_p = 38$ Å.

advantages of adsorptive CO_2 storages strategies versus compressed-fluid ones, emphasizing the greater efficiency of small, that is, subnanometer pores over larger mesopores as adsorption devices.[4,5,10,11] The global efficiency can be gauged from quantitative grounds by computing the average density inside the pore, namely,

$$\langle \rho_p \rangle = \frac{\int_0^R 2\pi r \rho(r)\, dr}{\int_0^R 2\pi r\, dr} \quad (3)$$

Results for $\langle \rho_p \rangle$ are presented in Figure 5a. The large and positive deviations of $\langle \rho_p \rangle/\rho_c$ with respect ρ_b/ρ_c at low bulk densities reveal the high adsorptive powers of the two pores. Moreover, in the two cases, the curves level off beyond $\rho_b/\rho_c \approx 0.2-0.5$ and remain practically constant for higher bulk densities. Interestingly these characteristics coincide with

DOI: 10.1021/acs.jpcc.5b09000
J. Phys. Chem. C XXXX, XXX, XXX−XXX

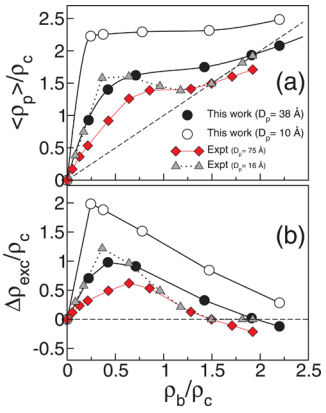

Figure 5. (a) Variation of CO_2 pore average density, $\langle\rho_p\rangle$, within simulated nanopores of size D_p = 38 and 10 Å, versus the bulk density. The dashed line corresponds to $\langle\rho_p\rangle \equiv \rho_b$ (zero sorption reference). (b) Excess density of confined $scCO_2$. Experimental data were taken from (red diamonds) ref 5, measured on 75 Å CPG-10 silica glass pores, and (gray triangles) from ref 4, measured in 16 Å micropores, at T = 308 K.

experimental information reported in refs 4 and 5. The plots that appear in the bottom panel correspond to the same set of results expressed now in terms of the excess densities, namely $\Delta\rho_{exc} = \rho_p - \rho_b$. Note that for ρ_b beyond $\sim \rho_c$, the global density inside the pore is less than that in the bulk, most probably due to steric restrictions arising from inefficient packing. Nevertheless, our results for D_p = 38 Å, still reproduce the experimental zero sorption bulk density remarkably well.

We also examined orientational correlations of the confined CO_2. The gross features of such correlations at the vicinity of the pore walls can be percieved from the three plots that appear in inset c in Figure 3. The curves correspond to profiles for local densities of the central O− and the distal C−groups. The almost perfect overlap between the set of curves suggests that CO_2 molecules in contact with the pore wall lie parallel to the solid substrate. To gain additional insight into these characteristics in inner regions, we examined the following distribution function:

$$P(\cos\theta) = \langle\delta(|\cos\theta_i| - \cos\theta)\rangle \tag{4}$$

where

$$\cos\theta_i = \frac{\mathbf{r}\cdot\hat{u}_i}{|\mathbf{r}|} \tag{5}$$

In the previous equation $\hat{\mathbf{u}}_i$ represents a unit axial vector along the O−O direction in the ith CO_2 molecule. In Figure 6a we present results for $P(\cos\theta)$ for the illustrative case of a 38 Å pore in contact with a supercritical CO_2 phase with ρ_b/ρ_c = 0.44. In this case, we discriminated three different pore-environments: the 3 Å width, outermost layer, an intermediate 11.5 Å ≤ r ≤ 15 Å cylindrical section, and a bulk like, r < 11.5 Å, inner region. The plot corresponding to the interfacial CO_2 (black circles) constrasts sharply with the other two and presents a clear maximum for cos θ = 0, in agreement with the previous observation based on the characteristics of the local site-densities. In the intermediate layer, one can still perceive a remnant of the propensity to parallel alignment while, in the "bulk"-like environment of the pore, the distribution exhibits a flat profile. Finally, we also looked into possible confinement effects on the relative orientations between neighboring molecules by computing the following correlation:

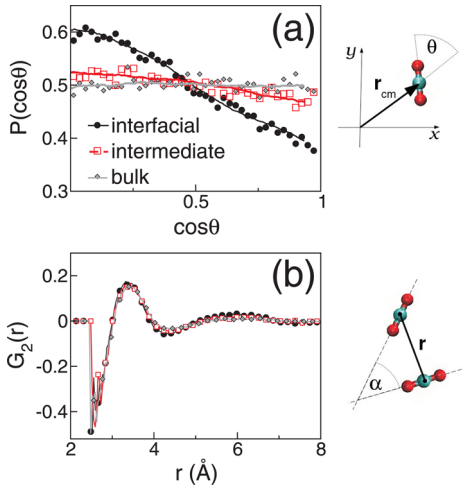

Figure 6. Orientational functions: (a) probability distribution $P(\cos\theta)$ as a function of the angle between the molecular axis and the center-of-mass radial vector, for the confined CO_2 molecules located within different regions, as indicated; (b) average of the second-order Legendre polynomial of the cosine angle between pairs of CO_2 confined molecules, as a function of the center-of-mass distance between them. All curves correspond to the system with ρ_b/ρ_c = 0.44.

$$G_2(r) = \frac{1}{N_{CO_2}}\langle\sum_{ij} P_2(\hat{u}_i\cdot\hat{u}_j)\delta(|\mathbf{r}_O^i - \mathbf{r}_C^j| - r)\rangle \tag{6}$$

where $P_2(x) = (3x^2 - 1)/2$ is the second-rank Legendre polynomial, $\hat{\mathbf{u}}_i$ denotes the unit vector along the O−O axis, and $\mathbf{r}_O^i$ represents the coordinate of the central O-site in the ith molecule. Values of $P_2(\cos\theta) = -0.5$ and $P_2(\cos\theta) = 1$ correspond to perfect T-shaped and slid-parallel configurations, respectively. Results for $G_2(r)$ are displayed in Figure 6b. At first glance, one observes no substantial differences between the results collected in different pore regions, a fact that would indicate that the intermolecular orientations are not affected by the presence of the silica interface in a significant fashion. On the other hand, $G_2(r)$ looks negative at short distances, denoting a preference for distorted T-shaped arrangements. This observation agrees with previous theoretical[28,29] and experimental studies[30,31] of pure $scCO_2$. At intermediate separations, $G_2(r)$ attains positive values close to $\sim$ 0.2, which would indicate that, on average, the O−O axes are oriented at an angle close to 65°, that is, midway between T-shaped and slid-parallel orientations.

Dynamical Properties. Before embarking in a detailed analysis of dynamical properties of trapped $scCO_2$ within the nanopores, it will be instructive to briefly examine the four panels composing Figure 7. In these panels we present the projected coordinates of the centers of mass of the trapped CO_2 molecules onto the pore wall, collected along a single, 9 ns trajectory, with temporal resolution of 20 ps. The projection was performed on an unrolled cylindrical surface of radius R. The vertical axes correspond to coordinates $l_i = R\phi_i$, where

$$\cos\phi_i = \frac{x_i}{\sqrt{x_i^2 + y_i^2}} \tag{7}$$

On the other hand, the abscissa axes coincides with axial directions of the cylindrical pores.

On the left-hand side, the two panels correspond to projections of CO_2 molecules in the outermost layer in contact with the pore walls; the other two, on the right-hand side,

DOI: 10.1021/acs.jpcc.5b09000
J. Phys. Chem. C XXXX, XXX, XXX−XXX

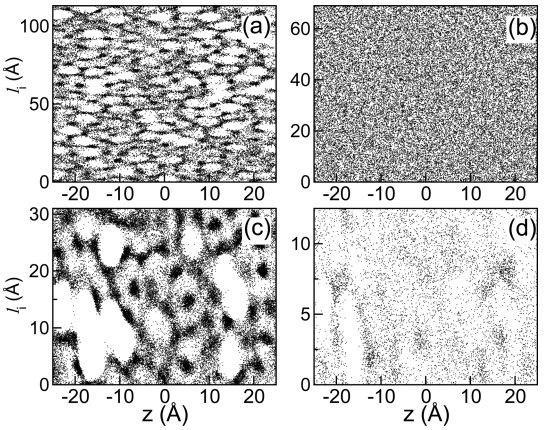

Figure 7. Projected center-of-mass coordinates of CO_2 onto cylindrical surfaces of radius R, along 9 ns trajectories, corresponding to $\rho_b/\rho_c = 1.44$. Upper and bottom panels correspond to the large and small pores, respectively. Panels a and c were generated considering the molecules within the adsorbed layer; whereas for panels b and d, the molecules lying within the most central region of the channel were taken into account.

correspond to projections of molecules in the "bulk"-like, central region of the pore. Clearly, the two sets of results contrast at a qualitative level: trajectories of external CO_2 molecules give rise to a set of irregular, "blank and dark" patches which are consistent with a strongly adsorbed layer, with severely hindered mobility. As such, the overall shape of the patchy structure should go hand-in-hand with the spatial characteristics of the rugosity of the underling solid wall. On the other hand, Figure 7 panels b and d show a different dynamical scenario: in wider pores, the points fill the projected surface uniformly, revealing standard, fluid-like dynamical characteristics of the diffusive motions. In narrower pores (panel d), the latter uniformity is somewhat less marked, due to the persistance of residual wall-dynamical-effects, down to center of the pore.

The previous observations can be gauged from a quantitative perspective by analyzing the translational mobility of the trapped CO_2 in terms of self-diffusion coefficients. Given the results shown in Figure 7, one can anticipate that CO_2 molecules inside the pore will present dynamical heterogeneities. Under these circumstances, it will be appropriate to define *local* diffusion coefficients expressed in terms of

$$D_{local}(r) = \frac{\mathcal{R}_r^2(t_2) - \mathcal{R}_r^2(t_1)}{6(t_2 - t_1).} \quad (8)$$

where $\mathcal{R}_r^2(t)$ represents the mean square displacement (MSD) of a tagged CO_2 molecule lying within a cylindrical, ringlike section of thickness Δr located at r. Note that the values of $\Delta t = t_2 - t_1$ should be chosen in order to ensure that (i) they are sufficiently longer than the time required for MSDs to reach their limiting, linear diffusive regimes and, at the same time, (ii) should be short enough to guarantee that the tagged CO_2 molecule remains within the same cylindrical shell, during the whole temporal interval Δt. We remark that, by setting $\Delta r = 1$ Å, $t_1 = 2$ ps, and $t_2 = 3$ ps, the previous conditions could be reasonably well satisfied. A similar analysis based on individual rotational times is straightforward. In this case, the rotational dynamics were analyzed in terms of the single-molecule autocorrelation function $C(t;r)$,

$$C(t) = \langle \hat{\mathbf{u}}_i(t) \cdot \hat{\mathbf{u}}_i(0) \rangle_r \quad (9)$$

where $\hat{\mathbf{u}}_i$ is the unit vector in the direction of the molecular axis of the ith CO_2 molecule lying in the cylindrical section centered at r. Moreover, local characteristic rotational times, $\tau_{local}(r)$, were obtained from the time interval necessary to observe the $C(\tau_{local};r) = 1/e$ decay.

The results for local diffusion coefficients and orientational relaxation times are displayed in Figure 8, normalized by the

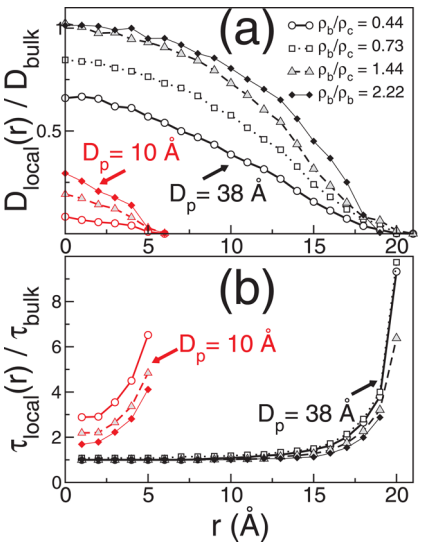

Figure 8. (a) Average diffusion coefficients and (b) average rotational correlation times of trapped $scCO_2$, normalized with the corresponding bulk values, as a function of the distance to the axial axis of the cylindrical pore. Results for the large and small pores are drawn in black and red, respectively, as indicated.

corresponding bulk values. As a distinctive feature, all diffusion coefficients exhibit sharp drops as r approaches the pore walls, regardless the particular bulk density considered. Note that the local diffusion at the central part of the D_p = 38 Å pore, becomes comparable that of the bulk ones, only for the systems with $\rho_b/\rho_c > 1$, whereas at intermediate and low densities, a reduction of the translational mobility is clearly observed even at the center of the pore. Within the small pores, self-diffusion coefficients of $scCO_2$ also display sharp drops at the pore walls, whereas at the centers, the corresponding values are between ~ 3 and 10 times smaller than that of the bulk. In all cases, the reduction of translational mobility at the center of the channels looks more marked at low CO_2 densities; this fact can be interpreted as a consequence of a propagation of a stronger interface-induced spatial ordering in layers that extend into the central region.

For the case of the largest pore, the rotational times depicted in Figure 8b look constant—and similar to the bulk rotational time—over a much broader region, away from the interface, although significant retardations are observed near the pore walls. These retardations at the interface seem to be somewhat milder as the fluid bulk density increases for both pore sizes.

Pore Functionalization. We will close our analysis by examining effects derived from the presence of different chemical functionalizations on the pore walls. In doing so, we will concentrate on a wide pore, in contact with a CO_2 supercritical phase with $\rho_b/\rho_c = 0.44$. Besides the already mentioned hydrophobic pore (Hpb), two additional types of

DOI: 10.1021/acs.jpcc.5b09000
J. Phys. Chem. C XXXX, XXX, XXX−XXX

channel functionalization were investigated: (i) a hydrophilic (Hpl) cavity, in which unsaturated oxygens were hydroxylated, leading to a surface density of SiOH groups of ~3 nm^{-2} (taken from ref 32) and (ii) an irregular, hydrophobic-like cavity, in which the silanol groups were replaced by trimethylsilyl groups, Si−O−Si-$(CH_3)_3$ (Hpb-TMS) protruding inward, toward the central part of the pore.

In Figure 9 we show results for local density profiles, $\rho(z)$. These densities were calculated according to eq 1, employing in

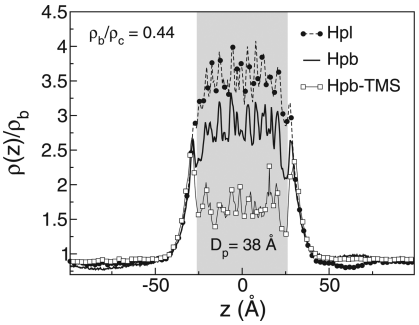

Figure 9. Local density of CO_2 along the pore axis, at T = 315 K and ρ_b/ρ_c = 0.44, for pores of diameter D_p = 38 Å and different functionalizations, as indicated by the labels.

all cases a global radius $R = D_p/2$. One observes a ~ 20% increment in the global density in Hpl pores, compared to the Hpb case; contrasting, the incorporation of TMS groups introduces the opposite effect yielding a global much more marked ~ 60% depletion of the original fluid density. The former effect can be rationalized in terms of a stronger adsorption affinity to the surface due to the presence of attractive Coulomb interactions between hydroxyl groups at the wall and distal sites in the supercritical fluid, similar, in spirit, to the one prevailing in hydrogen-bonded systems. On the other hand, the density reduction in the case of Hpb-TMS, could be adscribed to (i) first, a significant reduction of the available volume to accommodate CO_2 molecules inside the pore. Note that in the density calculation, we kept the global volume fixed at the original hydrophobic value. As such, the reduction in the density may also be due, in part, to the impossibility to compute the effective volume in the presence of the bulky TMS groups. (ii) Second, weaker effective interactions between disordered nonpolar methyl groups and CO_2 molecules.

Fluid structures within the different functionalized pores, along the radial coordinate are shown in Figure 10. The density enhancement in the Hpl case is also present along the radial profile, most notably considering the relative magnitudes of the interfacial maximum peaks in Hpl and Hpb pores. On the other hand, the density profile in the Hpb-TMS system shows substantial differences compared to the previous pores. The presence of TMS groups attached to the silica interface produces a dramatic depletion of the local fluid density in contact with the wall. In fact, one can still observe traces of the wall adsorption in a highly reduced peak at r ~ 17 Å that is indicative of the presence of scattered CO_2 molecules trapped within pockets flanked by TMS groups. Results for the average CO_2 density within the interior of each pore, obtained from eq 3 with R = 19.5 Å, yield $\langle\rho_p\rangle/\rho_c$ = 1.55, 1.35, and 0.82 for Hpl, Hpb, and Hpb-TMS systems, respectively. Given the characteristics of $\rho(r)$ for the Hpb-TMS system, the use of an effective radius close to $R \approx 15$ Å would be more adequate. In doing so,

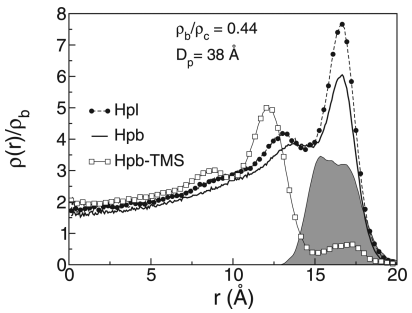

Figure 10. Local density of CO_2 along the radial axis, at T = 315 K and ρ_b/ρ_c = 0.44, for pores of diameter D_p = 38 Å and different functionalizations, as indicated by the labels. The shaded peak corresponds to the distribution of TMS groups in the Hpb-TMS system.

one obtains $\langle\rho_p^{Hpb-TMS}\rangle/\rho_c$ = 1.2, a value consistent with the direct extrapolation from the Hpl−Hpb trend.

IV. CONCLUSIONS

We investigated the structural and dynamical properties of supercritical CO_2 fluid confined within cylindrical silica nanopores of different size, by means of molecular dynamics simulations. Carbon dioxide's densities in the range ρ_b/ρ_c = 0.22−2.22 were simulated, along the supercritical isotherm T = 315 K, close to the critical temperature.

In agreement with previous experimental data obtained for CO_2 and other simple fluids,[5,10,33] we found that the trapped phase exhibits a dense phase, with higher density than the bulk fluid. Moreover, a simple hydrophobic-like silica surface, mimicked as a collection of dispersive Lennard-Jones sites, was able to reproduce the observed density enhancement at the interfacial region.

Radial density profiles revealed a fluid structure composed of concentrical layers at the vicinity of the inner pore walls. Radial profiles provide evidence for the presence of a first layer, strongly adsorbed at the interface, composed of CO_2 molecules oriented mostly parallel to the interface. The structure and behavior of this adsorbed fluid are only mildly sensitive to the bulk density at the reservoirs, and their characteristics are strongly associated with details in the topology and chemical properties of the interfacial species that constitute the pore wall. The excess density for confined CO_2 fluid exhibits a pronounced maximum at low bulk density. In particular, the value of this maximum was found to be larger for the smaller pores. Moreover, the location of this maximum density shifts toward larger values as the size of the pore is increased, in good agreement with experimental results.

At low bulk densities and tighter confinements, the average density of the confined fluid may exceed that of the bulk phase by a factor close to 5. In agreement with direct experimental information,[5] negative excess pore densities were registered at high bulk external densities, mainly due to inefficient packing inside the pore.

The analysis of the dynamics of $scCO_2$ within the pores, reveals that time scales of translational and rotational motions become significantly lengthened, when compared to values corresponding to bulk phases. The local dynamical analysis along the radial coordinate of the pore showed that these retardation effects become increasingly stronger at the vicinity of the pore walls. Moreover, these features are much more

DOI: 10.1021/acs.jpcc.5b09000
J. Phys. Chem. C XXXX, XXX, XXX−XXX

marked in smaller pores—with diameters comparable to or lower than ∼ 3 molecular lengths.

Finally, effects from different functionalizations of the pore walls on the CO_2 density were also analyzed for the larger pore at low bulk densities. Our results reveal that the density enhancement can be further incremented by hydroxylation of the silica surface. The presence of SiOH polar groups on the silica walls benefits in an additional 15% enhancement of the average density inside the pore, with respect to that in the simple hydrophobic, Lennard-Jones pore case. Contrasting, the irregular and hydrophobic-like surface functionalized with TMS groups produces a 40% reduction of the storage capacity of the pore.

Summarizing, the present study clearly demonstrates that adsorption and confinement are efficient ingredients in order to increase CO_2 storage capacities. The development of new functionalizations and synthesis protocols, focused on those properties, may be specifically designed in order to further improve the CO_2 storage capacities in porous materials.

AUTHOR INFORMATION

Corresponding Author

*E-mail: DoloresElola@gmail.com. Tel.: 54-11-6772-7046. Fax: 54-11-6772-7121.

Notes

The authors declare no competing financial interest.

ACKNOWLEDGMENTS

M.D.E. and J.R. are grateful for financial support from ANPCyT (Grant PICT 2013-1323) and CONICET (Grant PIP 112-201101-00464). M.D.E. and J.R. are staff members of CONICET, Argentina.

REFERENCES

(1) Steriotis, T. A.; Stefanopoulos, K. L.; Mitropoulos, A. C.; Kanellopoulos, N. K.; Hoser, A.; Hofmann, M. Structural Studies of Supercritical Carbon Dioxide in Confined Space. *Appl. Phys. A: Mater. Sci. Process.* **2002**, *74*, S1333−S1335.

(2) Rother, G.; Melnichenko, Y. B.; Cole, D. R.; Frielinghaus, H.; Wignall, G. D. Microstructural Characterization of Adsorption and Depletion Regimes of Supercritical Fluids in Nanopores. *J. Phys. Chem. C* **2007**, *111*, 15736−15742.

(3) Belmabkhout, Y.; Sayari, A. Effect of Pore Expansion and Amine Functionalization of Mesoporous Silica on CO_2 Adsorption Over a Wide Range of Conditions. *Adsorption* **2009**, *15*, 318−328.

(4) Melnichenko, Y. B.; Mayama, H.; Cheng, G.; Blach, T. Monitoring Phase Behabior of Sub- and Supercritical CO_2Confined in Porous Fractal Silica with 85% Porosity. *Langmuir* **2010**, *26*, 6374−6379.

(5) Rother, G.; Krukowski, E. G.; Wallacher, D.; Grimm, N.; Bodnar, R. J. "Pore Size Effects on the Sorption of Supercritical CO_2 in Mesoporous CPG-10 Silica. *J. Phys. Chem. C* **2012**, *116*, 917−922.

(6) Rother, G.; Vlcek, L.; Gruszkiewicz, M. S.; Chialvo, A. A.; Anovitz, L. M.; Bañuelos, J. L.; Wallacher, D.; Grimm, N.; Cole, D. R. Sorption Phase of Supercritical CO_2 in Silica Aerogel and Mesoscale Computer Simulations. *J. Phys. Chem. C* **2014**, *118*, 15525−15533.

(7) Stefanopoulos, K. L.; Steriotis, T. A.; Kanellopoulos, N. K.; Hannon, A. C.; Ramsay, J. D. F.; Katsaros, F. K. Structural Study of Supercritical Carbon Dioxide Confined in Nanoporous Silica by In-Situ Neutron Diffraction. *J. Phys.: Conf. Ser.* **2012**, *340*, 012049.

(8) Lastoskie, C. Caging Carbon Dioxide. *Science* **2010**, *330*, 595−596.

(9) Vaidhyanathan, R.; Iremonger, S. S.; Shimizu, G. K. H.; Boyd, P. G.; Alavi, S.; Woo, T. K. Direct Observation and Quantification of CO_2 Binding Within an Amine-Functionalized Nanoporous Solid. *Science* **2010**, *330*, 650−653.

(10) Gallego, N. C.; He, L.; Saha, D.; Contescu, C. I.; Melnichenko, Y. B. Hydrogen Confinement in Carbon Nanopores: Extreme Densification at Ambient Temperature. *J. Am. Chem. Soc.* **2011**, *133*, 13794−13797.

(11) Ciccariello, S.; Melnichenko, Y. B.; He, L. Phase Behavior of Carbon Dioxide Confined in Silica Aerogel in the Vicinity of the Bulk Critical Point. *J. Phys. Chem. C* **2011**, *115*, 22336−22346.

(12) Gruszkiewicz, M. S.; Rother, G.; Wesolowski, D. J.; Cole, D. R.; Wallacher, D. Direct Measurements of Pore Fluid Density by Vibrating Tube Densimetry. *Langmuir* **2012**, *28*, 5070−5078.

(13) Siemons, N.; Busch, A. Measurement and Interpretation of Supercritical CO_2 Sorption on Various Coals. *Int. J. Coal Geol.* **2007**, *69*, 229−242.

(14) Watson, G. C.; Jensen, N. K.; Rufford, T. E.; Chan, K. I.; May, E. F. Volumetric Adsorption Measurements of N_2, CO_2, CH_4 and a CO_2 + CH_4 Mixture on a Natural Chabazite from (5 to 3000) kPa. *J. Chem. Eng. Data* **2011**, *57*, 93−101.

(15) Qin, Y.; Yang, X.; Zhu, Y.; Ping, J. MD Simulation of Interaction Between Supercritical CO_2 Fluid and Modified Silica Surfaces. *J. Phys. Chem. C* **2008**, *112*, 12815−12824.

(16) Yang, X.; Xu, Z.; Zhang, C. MD Simulation of Dense Carbon Dioxide Fluid on Amorphous Silica Surfaces. *J. Colloid Interface Sci.* **2006**, *297*, 38−44.

(17) Yang, X.; Yue, X. Adsorption and Structure of Lennard-Jones Model Fluid in Slit-Like Amorphous Silica nanopores. *Colloids Surf., A* **2007**, *301*, 166−173.

(18) Ho, L. N.; Clauzier, S.; Schuurman, Y.; Farrusseng, D.; Coasne, B. Gas Uptake in Solvents Confined in Mesopores: Adsorption Versus Enhanced Solubility. *J. Phys. Chem. Lett.* **2013**, *4*, 2274−2278.

(19) Coasne, B.; Pellenq, R. J.-M. Grand Canonical Monte Carlo Simulation of Argon Adsorption at the Surface of Silica Nanopores: Effect of Pore Size, Pore Morphology and Surface Roughness. *J. Chem. Phys.* **2004**, *120*, 2913−2922.

(20) Harris, J. G.; Yung, K. H. Carbon Dioxide's Liquid-Vapor Coexistence Curve and Critical Properties as Predicted by a Simple Molecular Model. *J. Phys. Chem.* **1995**, *99*, 12021−12024.

(21) Rodriguez, J.; Elola, M. D.; Laria, D. Confined Polar Mixtures Within Cylindrical Nanocavities. *J. Phys. Chem. B* **2010**, *114*, 7900−7908.

(22) Elola, M. D.; Rodriguez, J.; Laria, D. Structure and Dynamics of Liquid Methanol Confined Within Functionalized Silica Nanopores. *J. Chem. Phys.* **2010**, *133*, 154707−154715.

(23) Elola, M. D.; Rodriguez, J.; Laria, D. Liquid Methanol Confined Within Functionalized Silica Nanopores. II: Solvation Dynamics of Coumarin 153. *J. Phys. Chem. B* **2011**, *115*, 12859−12867.

(24) Phillips, J. C.; Braun, R.; Wang, W.; Gumbart, J.; Tajkhorshid, E.; Villa, E.; Chipot, C.; Skeel, R. D.; Kale, L.; Schulten, K. Scalable MD with namd. *J. Comput. Chem.* **2005**, *26*, 1781−1802.

(25) Tucker, S. C. Solvent Density Inhomogeneities in Supercritical Fluids. *Chem. Rev.* **1999**, *99*, 391−418.

(26) Song, W.; Biswas, R.; Maroncelli, M. Intermolecular Interactions and Local Density Augmentation in Supercritical Solvation: A Survey of Simulation and Experimental Results. *J. Phys. Chem. A* **2000**, *104*, 6924−6939.

(27) Lewis, J. E.; Biswas, R.; Robinson, A. G.; Maroncelli, M. Local Density Augmentation in Supercritical Solvents: Electronic Shifts of Anthracene Derivatives. *J. Phys. Chem. B* **2001**, *105*, 3306−3318.

(28) Balasubramanian, S.; Kohlmeyer, A.; Klein, M. L. Ab Initio Molecular Dynamics Study of Supercritical Carbon Dioxide Including Dispersion Corrections. *J. Chem. Phys.* **2009**, *131*, 144506(1)−144506(4).

(29) Saharay, M.; Balasubramanian, S. Ab Initio Molecular Dynamics Study of Supercritical Carbon Dioxide. *J. Chem. Phys.* **2004**, *120*, 9694−9702.

(30) Chiappini, S. Neutron Diffraction Measurements on High Pressure Supercritical CO_2. *Mol. Phys.* **1996**, *89*, 975−987.

DOI: 10.1021/acs.jpcc.5b09000
J. Phys. Chem. C XXXX, XXX, XXX−XXX

(31) Cipriani, P.; Nardone, M.; Ricci, F. P. Neutron Diffraction Measurements on CO_2 in Both Undercritical and Supercritical States. *Phys. B* **1998**, *241−243*, 940−946.
(32) Kamijo, T.; Yamaguchi, A.; Suzuki, S.; Teramae, N.; Itoh, T.; Ikeda, T. Solvation Dynamics of Coumarin 153 in Alcohols Confined in Silica Nanochannels. *J. Phys. Chem. A* **2008**, *112*, 11535−11542.
(33) Do, D. D.; Do, H. D. Adsorption of Argon from Sub- to Supercritical Conditions on Graphitized Thermal Carbon Black and in Graphitic Slit Pores:A Grand Canonical Monte Carlo Simulation. *J. Chem. Phys.* **2005**, *123*, 084701−084715.

DOI: 10.1021/acs.jpcc.5b09000
J. Phys. Chem. C XXXX, XXX, XXX−XXX